Contact and edge effects in graphene devices

EDUARDO J. H. LEE[1]*, KANNAN BALASUBRAMANIAN[1], RALF THOMAS WEITZ[1], MARKO BURGHARD[1] AND KLAUS KERN[1,2]

[1]Max-Planck-Institute for Solid State Research, Heisenbergstrasse 1, D-70569 Stuttgart, Germany
[2]Institut de Physique des Nanostructures, École Polytechnique Fédérale de Lausanne, CH-1015 Lausanne, Switzerland
*e-mail: e.lee@fkf.mpg.de

Published online: 29 June 2008; doi:10.1038/nnano.2008.172

Electrical transport studies on graphene have been focused mainly on the linear dispersion region around the Fermi level[1,2] and, in particular, on the effects associated with the quasiparticles in graphene behaving as relativistic particles known as Dirac fermions[3–5]. However, some theoretical work has suggested that several features of electron transport in graphene are better described by conventional semiconductor physics[6,7]. Here we use scanning photocurrent microscopy to explore the impact of electrical contacts and sheet edges on charge transport through graphene devices. The photocurrent distribution reveals the presence of potential steps that act as transport barriers at the metal contacts. Modulations in the electrical potential within the graphene sheets are also observed. Moreover, we find that the transition from the p- to n-type regime induced by electrostatic gating does not occur homogeneously within the sheets. Instead, at low carrier densities we observe the formation of p-type conducting edges surrounding a central n-type channel.

Graphene is a zero-gap semiconductor and has a novel electronic structure, with its conduction and valence bands meeting at the Dirac point[2]. This characteristic enables the electrical transport to be tuned between hole or electron conduction by shifting the Fermi level with an applied electric field[1]. Graphene devices thus exhibit ambipolar behaviour, although with an unexpectedly high conductivity minimum[5]. This observation was recently explained by the formation of electron–hole puddles at the Dirac point, which arise from charged impurity centres[6,8–11]. However, in contrast to typical semiconductor devices in which the contacts are optimized in order to avoid scattering or reflection[12], the detailed properties of metal contacts with graphene (which might have significant implications for charge transport in such devices[13–15]) have not yet been explored. Another important aspect requiring further study is the influence of the boundaries of the sheets, which are expected to significantly influence charge transport, analogous to the formation of surface states in bulk semiconductors[12]. Here we use scanning photocurrent microscopy (SPCM) to explore these issues in graphene monolayers under different device operation conditions. SPCM has a spatial resolution on the order of 400 nm, which has previously proved sufficient to map the local electrostatic potential of devices containing carbon nanotubes and semiconductor nanowires[16–20].

For the SPCM measurements, graphene monolayers prepared by mechanical exfoliation[1] were contacted by Ti (0.3 nm)/Au (20 nm) electrodes on Si/SiO_2 substrates. The Si substrate is used as a backgate, with a 300-nm thermally grown oxide layer serving as the gate dielectric. Figure 1a shows an atomic force microscopy (AFM) image of a typical device used in this study. The height of the graphene sheet was determined to be approximately 1.1 nm, in good agreement with values reported for measurements performed in air[4]. Raman spectroscopy was also used to confirm that the samples comprised a single layer[21]. Four-probe measurements, although not ideal due to the invasive character of the contacts, indicated that the contacts significantly contribute to the total resistance of the devices (see Supplementary Information, Fig. S1). The two-probe drain current (I_d) measured at a constant drain-source bias ($V_{ds} = 1$ mV) as a function of gate voltage (V_{gs}) is displayed in Fig. 1b, where the typical ambipolar behaviour is visible.

SPCM was performed under ambient conditions by scanning the device through a diffraction-limited laser spot ($\lambda = 514.5$ nm, spot size $\sim$0.4 μm, power $\sim$100 kW cm^{-2}), and the reflected light and the photocurrent recorded simultaneously (see Supplementary Information, Fig. S2). The optical and photocurrent images were then processed by the WSxM package[22]. The reflection image (Fig. 1c) enabled the local origin of the photocurrent response within the device to be correlated. Figure 1d presents a photocurrent image taken at zero source–drain and zero gate bias, under which condition the device is close to the Dirac point. The image displays several photocurrent spots along the sheet, which indicate the presence of local built-in electric fields that induce a separation of photogenerated charge carriers analogous to observations on carbon nanotubes (CNTs)[16–19]. The existence of such local electric fields is in agreement with experimentally observed spatial potential fluctuations associated with the formation of electron–hole puddles[6,8]. Moreover, the possibility to generate photo-excited carriers in graphene is corroborated by recent Raman and visibility studies revealing the optical absorption of graphene at visible wavelengths[21,23–25].

In addition to the relatively weak photocurrent signals along the sheet, strong responses occur at the two metal contacts (Fig. 1d). Complete I_d–V_{ds} curves (shown in Fig. 1e) taken at the contacts under illumination provide evidence of the generation of an offset photovoltage of around 2 mV, with only a negligible

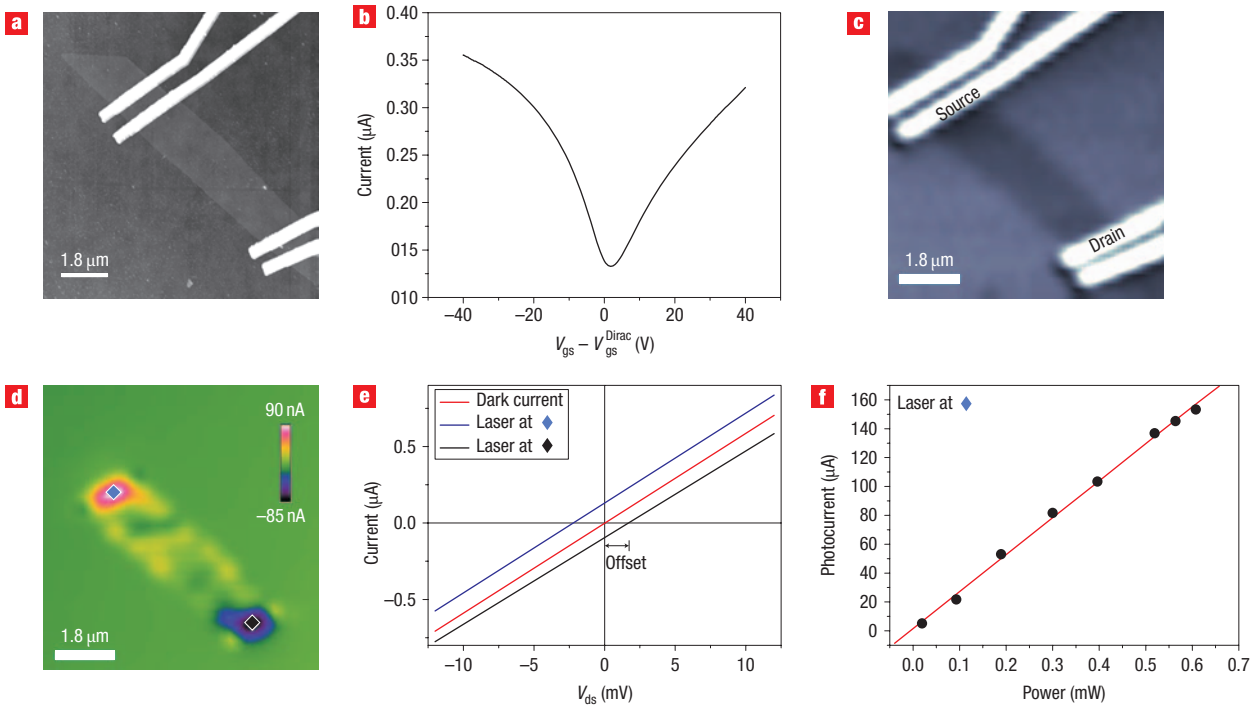

Figure 1 Photocurrent response of a graphene device. a, AFM image of a graphene monolayer contacted by four gold electrodes. **b**, Gate dependence of the drain current (I_d) measured at $V_{ds} = 1$ mV. **c**, Optical reflection image acquired simultaneously with the photocurrent image. The drain and source electrodes used in the measurements are indicated. **d**, Photocurrent image taken at $V_{ds} = V_{gs} = 0$ V. Further measurements were performed by fixing the laser spot at the positions marked by the black and blue diamonds. **e**, I_d–V_{ds} characteristics recorded in the dark, and with the laser positioned as marked in **d. f**, Photocurrent detected at the position marked by the blue diamond as a function of the laser power.

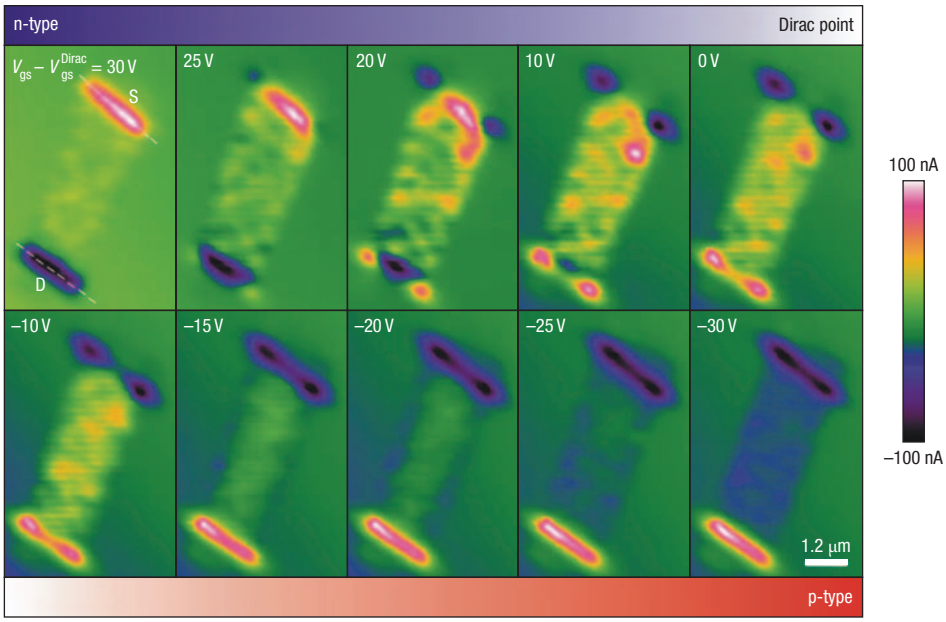

Figure 2 Spatially resolved photocurrent maps at various transport regimes of a graphene device. The sequence of images display the n- to p-type transition, as the gate voltage is swept from 30 to −30 V. The dashed lines in the top left image indicate the position of the drain (D) and source (S) electrodes.

resistance change of the device. Furthermore, the photocurrent at the contacts exhibits a linear dependence on the incident laser intensity, as depicted in Fig. 1f. These two findings can be attributed to the presence of electrostatic potential steps at the contacts[16–19]. According to recent theoretical work, a difference in the work functions of the metal and graphene leads to charge

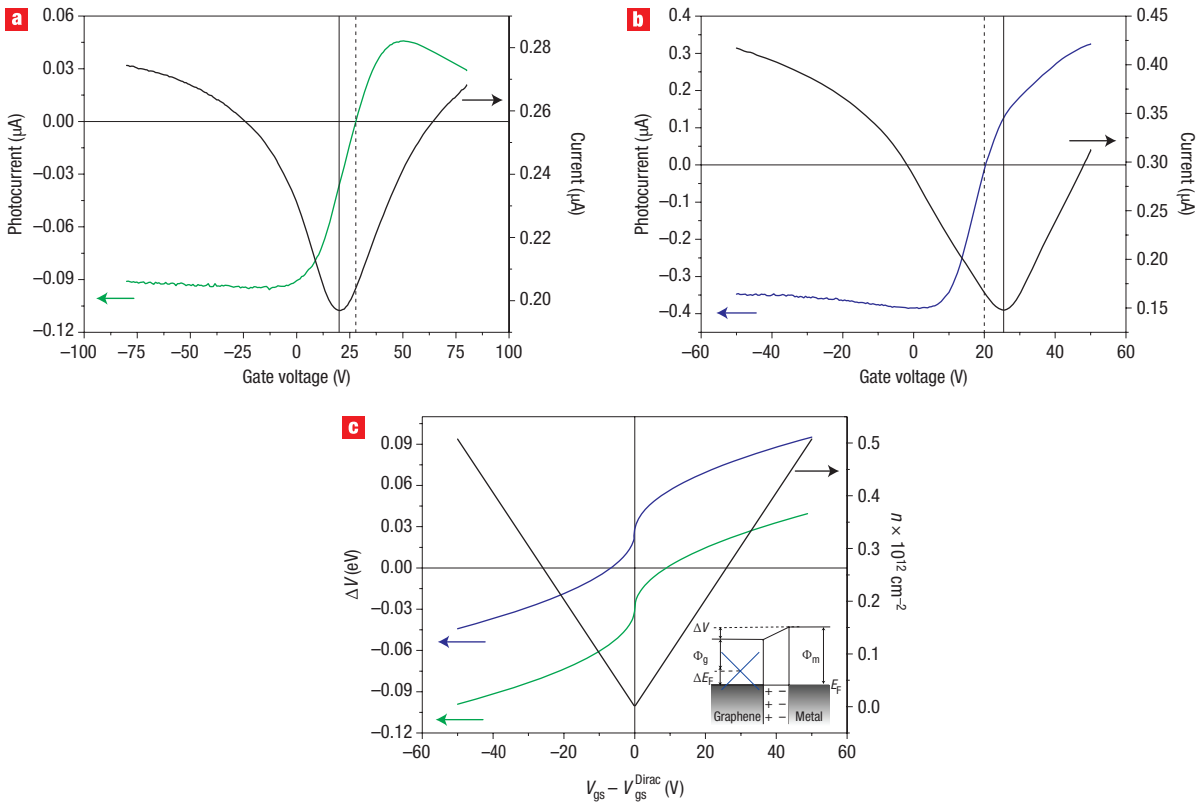

Figure 3 Quantitative determination of the potential steps at the metal–graphene interface. a,**b**, Gate dependence of the dark current measured with $V_{ds} = 1$ mV in **a** and $V_{ds} = 2$ mV in **b** (I_d; black lines) and the photocurrent at the metal–contact interface for Au-contacted devices (**a**, green) and for Ti-contacted devices (**b**, blue). **c**, Plot of the potential step at the metal–graphene interface, as described by equation (1), as a function of the gate voltage. The green and blue lines correspond to the cases of the Au- and Ti-contacted devices, respectively, where $\Phi_{Au} = 4.7$ eV and $\Phi_{Ti} = 4.3$ eV, and ΔE_F was obtained by fitting equation (1) to our experimental data. The black curve corresponds to the gate dependence of the charge carrier density. The inset schematically illustrates the energy level alignment at the metal-graphene interface, and the resulting Fermi level in graphene with respect to the Dirac point. The interfacial potential step is denoted as ΔV, ΔE_F corresponds to the Fermi level shift due to charge transfer from the contact, and Φ_g and Φ_m are the work functions of graphene and the metal contact, respectively.

transfer at the contact interface[13]. Owing to the low density of states in the vicinity of the Dirac point, this results in the formation of pronounced interface dipole layers. Such metal-induced doping has been reproducibly observed in the corresponding SPCM images of a wide range of samples.

Other interesting observations in Fig. 1d are the strong positive photoresponse at the centre of the source contact and strong negative photoresponse at the centre of the drain contact, and weaker negative and positive photocurrent lobes occurring at the electrode edges. In order to unravel the origin of this distribution, SPCM images were acquired in different transport regimes by varying the backgate voltage. Figure 2 displays such a sequence of zero bias photocurrent images covering the n- to p-type transition of a second device. The top left image, which belongs to the n-type regime, discloses that the photoresponse is dominated by the contacts, involving a positive photocurrent throughout the entire source–graphene interface and negative photocurrent throughout the drain–graphene interface. The corresponding photocurrent image taken in the p-type regime (right bottom image) is very similar, except for its opposite polarity, that is, positive photocurrent at the drain contact and negative at the source contact. The inverted photocurrent polarities in the two regimes demonstrate that the magnitude of the interfacial potential step changes with the gate potential. This dependence is highlighted in Fig. 3a, where the photocurrent detected at the centre of the source contact is plotted as a function of the gate voltage. The sign of the detected photocurrent is observed to reverse at $\sim V_{gs} = 28$ V, on the right side of the Dirac point (corresponding to minimum conductance). For comparison, we also studied devices with contacts made of a metal with lower work function (10-nm Ti covered by 5-nm Au). In contrast to the gold contact case, the latter devices exhibit the zero-current crossing on the left side of the Dirac point (Fig. 3b). In order to analyse this difference, we follow the approach of ref. 13 to express the potential step at zero gate voltage in terms of the work functions of the metal (Φ_M) and of graphene (Φ_G) and the Fermi level shift imparted by the metal doping on the graphene flake (ΔE_F), according to the scheme in Fig. 3c. When the gating-induced shift of the Fermi level is included, the potential step is given by

$$\Delta V = \Phi_M - \Phi_G - \Delta E_F + \mathrm{sgn}(V_{gs} - V_{gs}^{Dirac})\hbar v_F \sqrt{\pi\alpha}\sqrt{V_{gs} - V_{gs}^{Dirac}} \qquad (1)$$

where $\alpha = 7.2 \times 10^{10}\mathrm{cm}^{-2}\,\mathrm{V}^{-1}$ and $\hbar v_F = 5.52$ eVÅ (refs 1, 2, 26). By assuming a work function of $\Phi_{Ti} = 4.3$ eV for titanium, $\Phi_{Au} = 4.7$ eV (accounting for oxygen adsorption from the ambient[27]) for gold, and $\Phi_G = 4.5$ eV for graphene, the potential

step magnitude can be plotted as a function of the gate voltage and ΔE_F (see Supplementary Information, Fig. S3). Best agreement between the measured gate voltage differences between the zero-photocurrent crossing and the Dirac point is obtained with $\Delta E_F = -0.23$ eV and 0.25 eV for the Ti- and Au-contacted devices, respectively. Consistent with recent theoretical calculations[13], these values confirm that Ti contacts result in n-type doping of graphene and Au contacts in p-type doping, with carrier densities of 5.5×10^{12} electrons cm^{-2} and 6.5×10^{12} holes cm^{-2}, respectively. Furthermore, equation (1) yields values of −50 meV and 30 meV for the potential step at the gold/graphene and titanium/graphene interfacial potential steps at the Dirac point, respectively.

In addition to the contact regions, a gate-dependent modulation of photoresponse can also be observed along the graphene flake. Specifically, at higher carrier densities, a weak photocurrent compared to the contact regions occurs within the sheet, which is predominantly positive or negative with a few weak oscillations in the n- and p-type regimes, respectively. By contrast, closer to the Dirac point the relative photocurrent intensity within the sheet increases, and randomly distributed regions of positive and negative photocurrent emerge (see Fig. 1d). This characteristic indicates that at higher carrier densities, the local electric fields associated with the barriers at the contacts become substantially larger than the potential landscape within the graphene sheet. By contrast, at lower carrier densities, potential fluctuations associated with charged impurities gain importance, because the screening promoted by charge carriers in the graphene flake is reduced.

Furthermore, the course of the n- to p-type transition displays a nucleation of photocurrent signals of opposite sign (with respect to the signal detected at the centre of the electrodes) at the metal–graphene edge interfaces when the gate voltage is decreased starting from the n-type regime (see Fig. 2). The intensity of these edge signals rises as V_{gs} is further decreased, and approaches that at the centre of the electrodes when the Dirac point is reached. Hence, it can be concluded that in this gate voltage range, p-type transport prevails at the edges of the graphene sheet, but in the central region electron conduction is dominating. Homogeneous p-type conduction across the entire device, as reflected by coalescing of the edge lobes, requires decreasing V_{gs} past the Dirac point. The fact that the n- to p-type transition occurs at different values of V_{gs} for the edges and the central region of the sheet suggests an altered electronic structure at the edges, as expected from the symmetry breaking of the honeycomb lattice. Signatures of pronounced disorder and the existence of local electronic states have previously been detected at graphene edges by spatially resolved Raman and scanning tunnelling spectroscopy[23,28]. The overall device behaviour and the formation of transversal p-n-p profiles close to the Dirac point can be further visualized through electrostatic potential maps, obtained to a first approximation by integrating the photocurrent response (see Supplementary Information, Fig. S4).

The metal-induced doping of graphene evidenced by SPCM investigation raises the question as to the impact of electrodes that are kept at floating potential. As demonstrated in Fig. 4a for the same device as in Fig. 1, photocurrent signals of opposite polarity can be observed around the floating electrode located between the drain and source contacts. This observation is consistent with the introduction of a local potential dip displaying gradients of opposite signs at the two faces of the floating electrode. Upon switching the device from the p- to the n-type regime (Fig. 4b), the sign of the photoresponses is inverted, which can be explained by the carrier density being

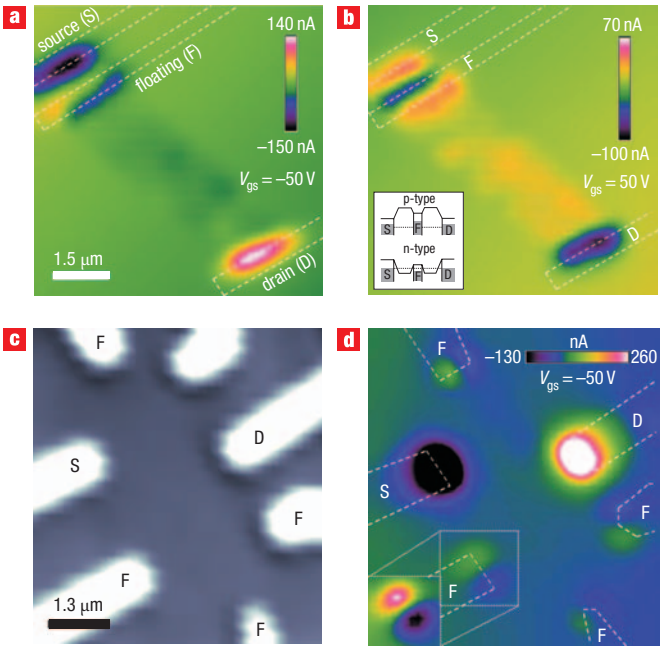

Figure 4 Invasive nature of metal contacts to graphene. a,**b**, Zero bias photocurrent images of the graphene device shown in Fig. 1, with the middle electrode kept at floating potential (F) at $V_{gs} = -50$ V and +50 V respectively. The inset shows a schematic of the electrostatic potential distribution around the floating electrode. **c**, Optical reflection image of a graphene multi-terminal device showing the source (S), drain (D) and floating (F) electrodes; the electrode without a label is not contacted to the graphene sheet. **d**, Photocurrent image of the device shown in **c**. The inset displays the photocurrent at the marked region, with a normalized colour scale to enhance contrast.

pinned below the floating electrode, while within the graphene it can be effectively modulated through the gate voltage. Similar signs of the invasiveness of metal contacts on graphene were observed on multi-terminal devices with floating electrodes at the periphery of the graphene flake, as depicted in Fig. 4c,d. In this case, although much stronger photoresponses appear at the drain and source electrodes, pairs of positive/negative photocurrent lobes can be discerned around all the floating electrodes.

In summary, the electrostatic potential landscape of graphene devices has been probed in different operation regimes. To this end, SPCM proved ideally suited to unravelling local changes in the electronic structure of the graphene sheets introduced by their interaction with deposited metal contacts and by local symmetry breaking/disorder at the sheet edges. These findings highlight the relevance of both material boundaries and contact interfaces in the operation of devices comprising two-dimensional nanostructures. For the future, spatially resolved photocurrent measurements are expected to provide valuable information regarding the effect of chemical doping and the development of multi-terminal graphene devices.

Received 23 April 2008; accepted 29 May 2008; published 29 June 2008.

References

1. Novoselov, K. S. *et al*. Electric field effect in atomically thin carbon films. *Science* **306,** 666–669 (2004).
2. Geim, A. K. & Novoselov, K. S. The rise of graphene. *Nature Mater.* **6,** 183–191 (2007).
3. Novoselov, K. S. *et al*. Two-dimensional gas of massless Dirac fermions in graphene. *Nature* **438,** 197–200 (2005).

4. Zhang, Y., Tan, J. W., Stormer, H. L. & Kim, P. Experimental observation of the quantum Hall effect and Berry's phase in graphene. *Nature* **438,** 201–204 (2005).
5. Katsnelson, M. I., Novoselov, K. S. & Geim, A. K. Chiral tunneling and the Klein paradox in graphene. *Nature Phys.* **2,** 620–625 (2006).
6. Hwang, E. H., Adam, S. & Das Sarma, S. Carrier transport in two-dimensional graphene layers. *Phys. Rev. Lett.* **98,** 186806 (2007).
7. Adam, S., Hwang, E. H., Galitski, V. M. & Das Sarma, S. A self-consistent theory for graphene transport. *Proc. Natl Acad. Sci. USA* **104,** 18392–18397 (2007).
8. Martin, J. *et al.* Observation of electron–hole puddles in graphene using a scanning single-electron transistor. *Nature Phys.* **4,** 144–148 (2008).
9. Tan, Y. W. *et al.* Measurement of scattering rate and minimum conductivity in graphene. *Phys. Rev. Lett.* **99,** 246803 (2007).
10. Rossi, E. & Das Sarma, S. Ground-state of graphene in the presence of random charge impurities. Preprint at <http://arxiv.org/abs/0803.0963> (2008).
11. Polini, M., Tomadin, A., Asgari, R. & MacDonald, A. H. Density-functional theory of graphene sheets. Preprint at <http://arxiv.org/abs/0803.4150> (2008).
12. Sze, S. M. *Physics of Semiconductor Devices* (Wiley, New York, 2007).
13. Giovannetti, G. *et al.* Doping graphene with metal contacts. Preprint at <http://arxiv.org/abs/0802.2267v2> (2008).
14. Golizadeh-Mojarad, R. & Datta, S. Effect of the contact induced states on minimum conductivity in graphene. Preprint at <http://arxiv.org/abs/0710.2727> (2007).
15. Huard, B., Stander, N., Sulpizio, J. A. & Goldhaber-Gordon, D. Evidence of the role of contacts on the observed electron–hole symmetry in graphene. Preprint at <http://arxiv.org/abs/0804.2040v1> (2008).
16. Balasubramanian, K. *et al.* Photoelectronic transport imaging of individual semiconducting carbon nanotubes. *Appl. Phys. Lett.* **84,** 2400–2402 (2004).
17. Balasubramanian, K., Burghard, M., Kern, K., Scolari, M. & Mews, A. Photocurrent imaging of charge transport barriers in carbon nanotube devices. *Nano Lett.* **5,** 507–510 (2005).
18. Lee, E. J. H. *et al.* Electronic band structure mapping of nanotube transistors by scanning photocurrent microscopy. *Small* **3,** 2038–2042 (2007).
19. Freitag, M. *et al.* Imaging of the Schottky barriers and charge depletion in carbon nanotube transistors. *Nano Lett.* **7,** 2037–2042 (2007).
20. Ahn, Y., Dunning, J. & Park, J. Scanning photocurrent imaging and electronic band studies in silicon nanowire field effect transistors. *Nano Lett.* **5,** 1367–1370 (2005).
21. Ferrari, A. C. *et al.* Raman spectrum of graphene and graphene layers. *Phys. Rev. Lett.* **97,** 187401 (2006).
22. Horcas, I. *et al.* WSxM: a software for scanning probe microscopy and a tool for nanotechnology. *Rev. Sci. Instrum.* **78,** 013705 (2007).
23. Graf, D. *et al.* Spatially-resolved Raman spectroscopy of single- and few-layer graphene. *Nano Lett.* **7,** 238–242 (2007).
24. Blake, P. *et al.* Making graphene visible. *Appl. Phys. Lett.* **91,** 063124 (2007).
25. Roddaro, S., Pingue, P., Piazza, V., Pellegrini, V. & Beltram, F. The optical visibility of graphene: interference colours of ultrathin graphite on SiO_2. *Nano Lett.* **7,** 2707–2710 (2007).
26. Piscanec, S., Lazzeri, M., Mauri, F., Ferrari, A. C. & Robertson, J. Kohn anomalies and electron–phonon interactions in graphite. *Phys. Rev. Lett.* **93,** 185503 (2004).
27. Hansen, W. N. & Johnson, K. B. Work function measurements in gas ambient. *Surf. Sci.* **316,** 373–382 (1994).
28. Klusek, Z. *et al.* Local electronic edge states of graphene layer deposited on Ir(111) surface studied by STM/CITS. *Appl. Surf. Sci.* **252**, 1221–1227 (2005).

Supplementary Information accompanies this paper at www.nature.com/naturenanotechnology.

Acknowledgements

The authors gratefully thank J. Smet and D. Obergfell for help with the preparation of the graphene monolayers, and A. Forment-Aliaga and A. Sagar for the Raman spectroscopy measurements.

Author information

Reprints and permission information is available online at http://npg.nature.com/reprintsandpermissions/.
Correspondence and requests for materials should be addressed to E.J.H.L.